Aerospace Science and Technology 168 (2026) 110858

Contents lists available at ScienceDirect

Aerospace Science and Technology

journal homepage: www.elsevier.com/locate/aescte

Original article

Assessing the accuracy of Radar-Plasma signature simulations using hypersonic shock-tunnel data with variable freestream oxygen levels

René Petervari [a,*], Stephan Weidner [b], Konstantinos Psarras [a], Flavien Denis [b], Peter Knott [a,c]

[a] Fraunhofer Institute for High Frequency Physics and Radar Techniques FHR, Fraunhoferstraße 20, Wachtberg, 53343, Germany
[b] Aerodynamics, Measurements and Simulations, French-German Research Institute of Saint-Louis (ISL), 5 rue du Général Cassagnou, Saint-Louis, 68300, France
[c] Radar Systems Engineering, Institute of High Frequency Technology (IHF), RWTH Aachen University, Melatener Straße 25, Aachen, 52056, Germany

ARTICLE INFO

Keywords:
Plasma sheaths
Radar signature
Aerospace simulation
Radar measurements
Wind tunnels
CFD
CEM

ABSTRACT

The plasma generation in hypersonic flight is known to affect the radar signatures of flight vehicles as well as their communications and sensing (radio blackout). Although these effects have been known since the beginning of spaceflight in the 1950s, accurate prediction is still difficult. Today, the most promising approach is to combine Computational Fluid Dynamics (CFD) and Computational Electromagnetics (CEM) to solve the plasma distribution in the flow field and derive the respective microwave response based on the two major plasma parameters: plasma and collision frequency. But dedicated experimental reference data is extremely scarce, which renders the validation of the multi-model dependent CFD-CEM approach difficult. To improve the validation, this study provides new experimental shock-tunnel radar data of the stagnation-point plasma of a 15 cm diameter sphere. To vary plasma and collision frequency independently, both the flow enthalpy and the freestream oxygen level were varied. The measurements are compared with respective CFD-CEM simulations.

1. Introduction

Since the early days of spaceflight, it is known that microwave communication and sensing is disturbed by a plasma sheath that emerges around a vehicle in hypersonic flight [1,2]. The two major areas of application are communication and sensing through the plasma sheath summarized under the terms radio blackout and radar sensing of hypersonic vehicles. The underlying physics are the same. However, despite years of research, there is still considerable uncertainty on when and where these effects occur and how strong they are [3,4]. A central reason is certainly that the plasma sheath depends not only on the flight state (angle-of-attack, speed, altitude, etc.) [1,5] but also on the shape and the material of the vehicle hull [6,7] making general conclusions difficult. But, even if all of these parameters were perfectly controllable, considerable modeling uncertainties remain that complicate the prediction of the plasma distribution and the respective microwave scatter.

Today's preferred approach to solve the microwave scatter at plasma sheathed objects is the combination of CFD and CEM simulations, see e.g. [3,4,6,8,9]. First, the plasma distribution is solved by CFD. Here, major uncertainties arise from the prediction of number densities of atoms, molecules, ions and electrons. The direct experimental measurement of such microscopic quantities is difficult leaving respective CFD predictions often unvalidated. As a consequence, accurate predictions of the plasma state in hypersonic flight are still an active field of research [10–14]. With the CFD data, the microwave scatter is predicted by a subsequent CEM simulation. The electromagnetic properties of the plasma sheath are derived from the CFD solution by using the Drude model for the plasma dispersion (for details see Section 2.2). In the absence of a magnetic field, it only incorporates the two parameters, plasma and collision frequency, which can be derived directly from the microscopic quantities predicted by CFD. Hence, the prediction of microwave scatter and thus also radar cross-sections (RCS) depends predominantly on an accurate prediction of microscopic quantities by CFD and the incorporated models.

However, while the plasma frequency (9) is well-defined, the calculation of the collision frequency (10) is rather unclear and lacks reference data for validation. Some authors use empirical relations [15–17] while others including the authors of this article follow a more rigorous approach relying on collision cross-sections derived to describe diffusion and viscosity in hypersonic flows [4,9,18]. Experimental reference data is necessary to reduce these uncertainties to a reasonable extent.

Facing similar modeling difficulties [19], in the 1960s and 1970s the U.S. missile defense program sponsored several ground test campaigns to address the problem experimentally [20–22]. The obtained

* Corresponding author.
E-mail address: rene.petervari@fhr.fraunhofer.de (R. Petervari).

https://doi.org/10.1016/j.ast.2025.110858
Received 19 May 2025; Received in revised form 15 July 2025; Accepted 28 August 2025
Available online 8 September 2025

Nomenclature

Parameter	Description
$\{\ \}_B, T^*, b_0, \lambda_D$	Bottin correlation parameters; [-]
$\{\ \}_G$	Gupta correlation parameters; [-]
B	bandwidth; [Hz]
c	speed of light; [m s^{-1}]
d	receive signal; [V]
d_s	shock standoff distance; [m]
D	Fourier receive signal; [V]
E	amplitude spectrum; [m^2]
e	electron charge; [C]
$\mathcal{F}$	Fourier trf.; [-]
F_s	CGI safety margin; [-]
f	radar frequency; [Hz]
f_c	(electron) collision frequency; [Hz]
f_p	(electron) plasma frequency; [Hz]
h	specific enthalpy; [MJ kg^{-1}]
H	transfer function; [m^2]
k_B	Boltzmann's constant; [kg m^2 s^{-2} K^{-1}]
m_e	electron mass; [kg]
$n(s)$	number density of species s; [m^{-3}]
M	heavy third body; [-]
Ma	Mach number; [-]
p	static pressure; [Pa]
p_{grid}	CGI convergence order; [-]
q	quantity; [-]
r	distance; [m]
r_{grid}	CGI refinement ratio; [-]
s	particle species; [-]
S	number of species; [-]
T_0	total/stagnation temperature; [K]
T_e	electron temperature; [K]
T_P	Park's temperature; [K]
T, T_{tr}	translational-rotational temperature; [K]
T_{ve}	vibrational-electronic temperature; [K]
u	velocity; [m s^{-1}]
$\bar{v}_e$	average electron velocity; [m s^{-1}]
w	waveform; [V]
W	Fourier trf. waveform; [V]
x, y, z	spatial coordinates; [m]
ϵ	CGI error; [-]
ϵ_0	electric field constant; [A s V^{-1} m]
ϵ_r	relative permittivity; [-]
ρ	density; [g m^{-3}]
$\bar{\Omega}^{(1,1)}_{ei}$	electron collision cross-sections; [m^2]
$\{\ \}_\infty$	freestream property; [-]
Σ	impulse response; [V]

data, however, remained often proprietary and if not it often lacks necessary information to reproduce the results.

In order to improve this situation with today's methods, a series of shock-tunnel experiments has been conducted in ISL's shock-tunnel laboratory [3]. The front reflection RCS of a hollow, dielectric 15 cm sphere in a hypersonic air flow was measured in the 3 GHz to 15 GHz range at freestream enthalpies ranging between 4 MJ kg^{-1} and 8 MJ kg^{-1}. Within the measurement uncertainty good agreement between the measured and simulated front reflection RCS was found. But, testing and validating a multi-dimensional model like the Drude model (Section 2.2), which is under test here, demands not only to vary a single parameter but rather a set of parameters to exclude systematic errors. Therefore, in this study, besides the enthalpy also the oxygen level in the freestream composition was varied (between 10 vol%,15 vol%, 21 vol% and 30 vol%) that affects both the plasma and the collision frequency and leads to different ratios of these. For each experiment, CFD-CEM simulations were conducted and compared with the measured RCS data using the model proposed in [23].

2. Theory

2.1. Aerodynamic model

For temperatures above 800 K, the polyatomic molecules in the air are vibrationally excited [24]. Therefore, the fluid does not behave like a calorically perfect gas—i.e. the specific heats are no longer constant but depend on the temperature. Additionally, the vibrational excitation state needs a higher number of molecular collisions to equilibrate compared to the translational and rotational energies of the molecules. At low densities, as in the present study, this can result in a thermal state, where the temperature based on the vibrational excitation differs from the temperature based on the translational and rotational energy of the molecules [25]. To model this behavior, [26] proposed a two-temperature model, where the translational and rotational as well as the vibrational and electronic energy modes are pooled together in a single translational–rotational and a single vibrational–electronic energy pool. The energy transfer between vibrational–electronic and translational–rotational energy modes is modeled utilizing the Landau–Teller equation and the corresponding relaxation time is obtained by the Millikan–White semi-empirical correlation [27] with Park's correction [26]. The energy transfer between electrons and heavy particles is modeled by the Appleton–Bray rate equation [28].

Furthermore, at temperatures in excess of 2000 K—as they do appear in the present study—oxygen molecules dissociate [24]. Hence, air can no longer be considered a fluid with fixed species concentrations. The changes of the species concentrations can be described by a chemical model. Previous studies [3,29] have shown that a 7-species air model based on [26] is capable of predicting species concentrations in the present flow fields. The same 7-species model comprising the chemical species {N2, O2, N, O, NO, NO+, e-} and the chemical reactions

$$\mathrm{N2 + M <=> [T_P][T_{tr}]2N + M,} \tag{1}$$

$$\mathrm{O2 + M <=> [T_P][T_{tr}]2O + M,} \tag{2}$$

$$\mathrm{NO + M <=> [T_P][T_{tr}]N + O + M,} \tag{3}$$

$$\mathrm{NO + O <=> [T_{tr}][T_{tr}]O2 + N,} \tag{4}$$

$$\mathrm{N2 + O <=> [T_{tr}][T_{tr}]NO + N,} \tag{5}$$

$$\mathrm{N + O <=> [T_{tr}][T_{ve}]NO + +e-,} \tag{6}$$

$$\mathrm{N2 + e- <=> [T_{ve}][T_{ve}]2N + e-,} \tag{7}$$

with M denoting a third body out of the heavy particles {N2, O2, N, O, NO, NO+} has been used in the present study. The reaction rates are calculated by the Arrhenius equation with the translational–rotational temperature T_{tr}, the vibrational–electronic temperature T_{ve} or Park's temperature $T_P = T_{tr}^{0.7} T_{ve}^{0.3}$ [26] depending on the reaction and its direction, as proposed by [30], and tabulated rate coefficients from [26]. The diffusion of the individual species is modeled by Fick's diffusion law and curve-fitted collision cross-sections from [31].

The individual thermal conductivity and shear viscosity of each species is calculated by the model of Blottner and Eucken [32]. Afterwards, the thermal conductivity and shear viscosity of the species mixture is determined by the mixing rules of Armaly and Sutton [33].

The described physico-chemical model has also been used in previous studies [3,29] and was able to predict electron number densities, pressures and shock-standoff distances within the experimental uncertainties.

2.2. Electromagnetic model

Since the electromagnetic plasma model has been thoroughly examined in previous works [3,23], it will only be briefly summarized here.

In the microwave spectrum pertinent to radar scattering, plasma can be modeled as a lossy dielectric medium [34, p.136]. Its permittivity ϵ_r depends on the plasma frequency f_p, the collision frequency f_c, and the microwave frequency f:

$$\epsilon_r = 1 - \frac{f_p^2}{f^2(1 - j\frac{f_c}{2\pi f})}. \tag{8}$$

This dispersion relation is also known as the Drude model. The electron plasma frequency is defined by:

$$f_p = \frac{1}{2\pi}\sqrt{\frac{n(e^-)e^2}{\epsilon_0 m_e}}, \tag{9}$$

where $n(e^-)$ and ϵ_0 denote the electron number density and the vacuum permittivity, while e and m_e represent the charge and mass of an electron. To model the collision frequency, a method incorporating collisional cross-sections $\bar{\Omega}_{ei}^{(1,1)}$ is employed:

$$f_c = \sum_{s=1}^{S} n(s)\bar{v}_e \pi \bar{\Omega}_{ei}^{(1,1)}, \tag{10}$$

$$\bar{v}_e = \sqrt{\frac{8k_B T_e}{\pi m_e}}. \tag{11}$$

This expression accounts for all collisions with particles of the S included species. The other key parameters are the average thermal velocity of electrons $\bar{v}_e$ and the number density $n(s)$ of species s. While multiple approaches exist for calculating the collision frequency and a consensus has yet to be reached, this method is promising as it is a standard technique for predicting other collision-dominated processes—viscosity and diffusion—in aerothermodynamic applications [35]. This approach has also been recently adopted by other researchers in the field, such as [4,9,18]. Besides the tabulated collision-cross sections from Gupta (in Å^2)

$$\pi\bar{\Omega}_{ei,Gupta}^{(1,1)} = e^{D_G} T^{A_G(\ln T)^2 + B_G \ln T + C_G}, \tag{12}$$

with A_G, B_G, C_G and D_G tabulated in [35], Bottin provides an alternative correlation. For charged-neutral or neutral-neutral collisions it states (in Å^2)

$$\pi\bar{\Omega}_{ei,Bottin}^{(1,1)} = e^{[[[A_B \cdot \ln(T)+B_B]\ln(T)+C_B]\ln(T)+D_B]} \tag{13}$$

and for charged-charged collision it states (in m^2)

$$\pi\bar{\Omega}_{ei,Bottin}^{(1,1)} = \frac{\pi\lambda_D^2}{T^{*2}} e^{[[[[A_B \cdot \ln(T^*)+B_B]\ln(T^*)+C_B]\ln(T^*)+D_B]\ln(T^*)+E_B]}, \tag{14}$$

$$T^* = \frac{\lambda_D}{2b_0}, \quad \lambda_D = \sqrt{\frac{\epsilon_0 k_B T}{2n(e^-)e^2}}, \quad b_0 = \frac{e^2}{8\pi\epsilon_0 k_B T}.$$

with A_B, B_B, C_B, D_B and E_B tabulated in [36].

3. Experiment

3.1. ISL's shock-tunnel laboratory

The experiments were conducted at ISL's shock-tunnel laboratory. The shock-tunnel B (STB) can provide enthalpies up to 8 MJ kg^{-1} for high enthalpy flow experiments [37]. This is achieved by filling the driver tube with highly pressurized hydrogen until a few mm thick metal diaphragm ruptures and causes a shock wave to run down the shock tube filled with the test gas as shown in Fig. 1. The shock wave is reflected at the end of the shock tube and creates the reservoir conditions with enthalpies up to 8 MJ kg^{-1}. The hot, pressurized gas ruptures and partly vaporizes a second plastic membrane and enters the formerly evacuated convergent-divergent Laval nozzle at subsonic speed. The characteristic shape of the nozzle produces the desired hypersonic test conditions at the nozzle exit. The effective test time with stationary high enthalpy flow conditions generally amounts to a few 100 µs. For the present experiments, the oxygen level in the test gas was varied between 10 vol% and 30 vol%. More details can be found in [3,37].

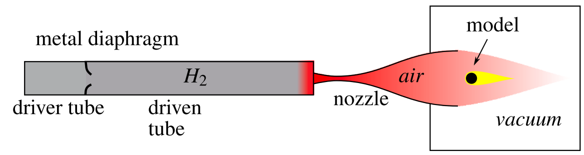

Fig. 1. Scheme of the wind tunnel during operation.

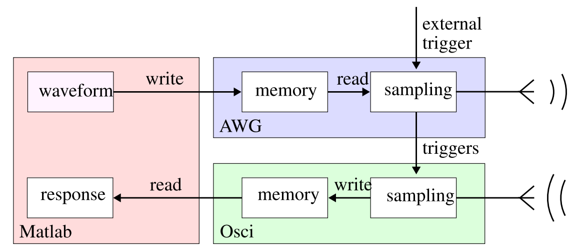

Fig. 2. MaSoDeRa system scheme.

3.2. The multi-application software defined Radar system

To measure the RCS during the wind tunnel test time, FHR's Multi-application Software Defined Radar (MaSoDeRa) system was used. An operation scheme is shown in Fig. 2. The system consists of an arbitrary waveform generator (AWG, Tektronix AWG70001) which samples the transmit signal directly. From here, it propagates through transmission lines to an antenna and is transmitted into space. At the same time a high performance oscilloscope (Osci, Tektronix DPO70000SX ATI) attached to a second antenna receives the incoming radiation. Both systems sample at a rate of 50 GS s^{-1} facilitating frequencies up to 20 GHz. Waveform definition and post processing is conducted in Matlab. The digitized incoming radiation d is a convolution of the transmitted waveform w with the impulse response Σ of the illuminated scene

$$d(t) = w(t) * \Sigma(t) \quad \Rightarrow \quad D(f) = W(f) \cdot \mathcal{F}(\Sigma(t))(f). \tag{15}$$

With the knowledge of the transmit waveform the impulse response of the scene as a function of time can be measured by

$$\Sigma(t) = \mathcal{F}^{-1}\left(\frac{D(f)}{W(f)}\right). \tag{16}$$

Since microwaves in free space propagate at the speed of light this time series can be interpreted as a range profile. For wind tunnel testing the system operates with a 3 to 15 GHz Linear Frequency Modulation (LFM) waveform in a high Pulse Repetition Frequency (PRF) mode and produces range profiles at a rate of 250 kHz. In the absence of plasma, this setup yields a range resolution of 1.25 cm. While this generates large data streams and the buffer memory size limits the observation time to a maximum of 10 ms, this is still sufficient for a maximum test duration of 200 µs. The used setup and calibration procedures are given below.

3.3. Setup and calibration

For this study the setup from [3] was used as baseline: a vertically polarized transmit and receive antenna pair was placed on top (Tx1 and Rx1) of the nozzle exit pointing towards the test section center. To improve the accuracy and increase the amount of data, the setup was extended by a second antenna pair with broadside view (Tx2 and Rx2) with horizontal polarization. The angles are measured from the center of the sphere to the center of the antenna pair (Fig. 4) and are listed in Table 1. Vertical and horizontal cross-sections are given in Figs. 5 and 6.

A hollow 150 mm diameter sphere made of polyamide (PA) was suspended onto the tunnel axis with its front 300 mm behind the nozzle exit and into the focus of the two antenna pairs. CFD simulations showed that this way the relevant stagnation region remained in the core flow

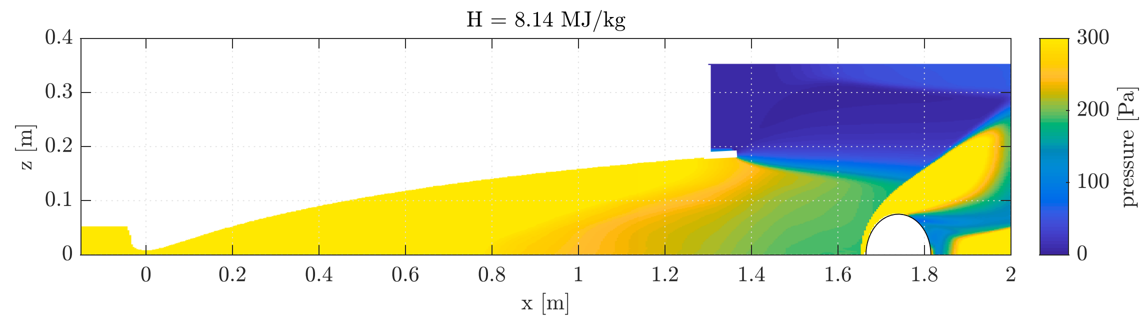

Fig. 3. Example distribution of the simulated pressure.

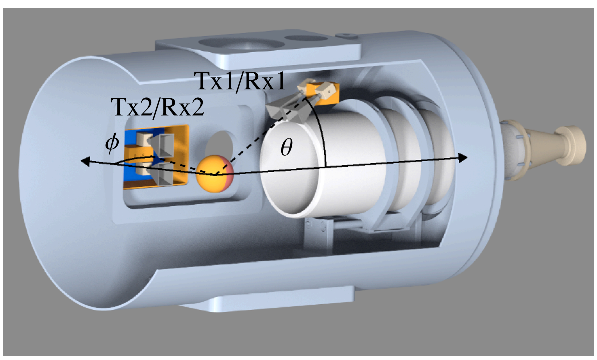

Fig. 4. 3D scheme of the test section setup.

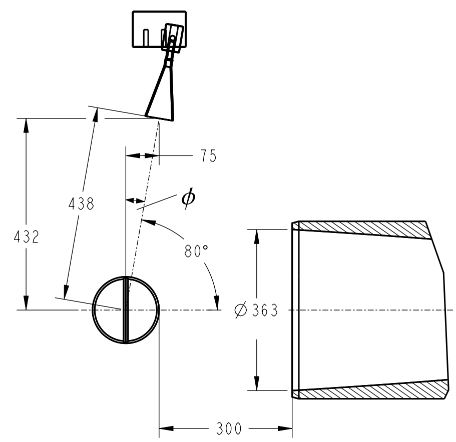

Fig. 6. Horizontal cross-section of the setup. Units in mm.

Table 1
The antenna angles.

Antenna	θ	ϕ
Tx1	34°	103°
Rx1	32°	82°
Tx2	−7°	9°
Rx2	7°	11°

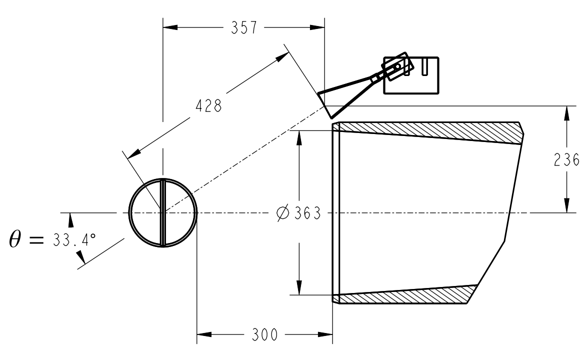

Fig. 5. Vertical cross-section of the setup. Units in mm.

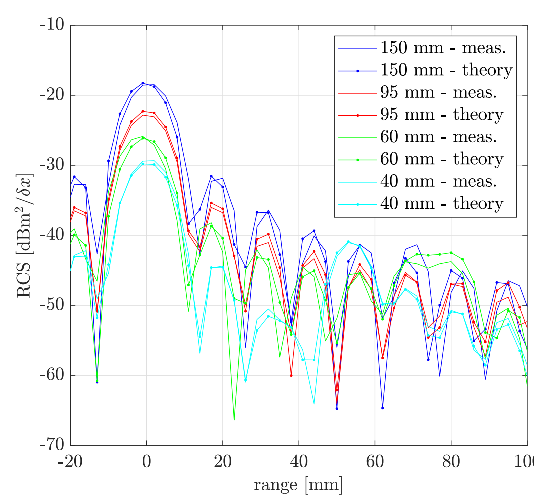

Fig. 7. Effect of the application of the transfer function to the measured metal sphere data exemplarily for the Tx1/Rx1 channel.

(Fig. 3). In lack of a precise positioning system, the sphere position could not be adjusted accurately before in [3] and varied between 230 mm and 256 mm. Hence, to improve the positioning accuracy and further reduce the uncertainty, the antenna position and orientation was measured precisely and a more dedicated suspension mechanism was designed and installed. To further reduce multi-path scatter and overall background scatter, the whole test section was covered with broadband microwave absorber foam.

To calibrate the MaSoDeRa system a set of four metallized spheres (diameters: 38 mm, 60 mm, 95 mm, 150 mm) were suspended into the antennas' mainbeam focus at 340 mm downstream of the nozzle exit. The transfer function $H(f)$ was derived from the measured data of the i-th sphere $E^i_{meas}(f)$ following the procedure in [3]

$$H(f) = \frac{1}{4}\sum_{i=1}^{4} \frac{E^i_{theory}(f)}{E^i_{meas}(f) r_i^2}, \tag{17}$$

where $E^i_{theory}(f)$ denote the analytical solution (Mie series) for bistatic backscatter of the i-th sphere in the frequency domain and r the distance from the specular reflection of the sphere and the antenna phase center. The calibrated range profiles of the sphere are shown exemplarily for Tx1Rx1 in Fig. 7. The obtained transfer function produces good agreement between measurement and analytical solution—especially when considering the peak value and the sidelobe structure. For convenience, the RCS values are corrected by the padding ratio [3]

$$\mathcal{F}(\Sigma^2)\ \ [\mathrm{m}^2] \quad \rightarrow \quad \eta\mathcal{F}(\Sigma^2)\ \ [\mathrm{m}^2/\delta r], \tag{18}$$

with η and $\delta r = \frac{c}{2B}$ as the padding ratio and the physical resolution, such that the peak value approximates the mean RCS in the considered frequency range if there is only one dominant peak—here the geometric cross-section of the respective sphere.

3.4. Test conditions

This study has the objective to investigate the accuracy of the current CFD-CEM model. As mentioned before, the electromagnetic properties of a plasma sheath depend predominantly on the plasma and collision frequency distribution. To separate the influence of each parameter and thus test this model (8), plasma and collision frequency must be varied independently. For this purpose we vary the flow enthalpy and the oxygen-nitrogen ratio of the test gas. In the STB shock-tunnel, higher enthalpies are accompanied by lower densities and higher temperatures. Since nitrogen ($14\,\mathrm{g\,mol^{-1}}$) is lighter than oxygen ($16\,\mathrm{g\,mol^{-1}}$), a reduction of the oxygen level reduces the weight of the test gas and increases the shock speed in the shock tube resulting in higher temperatures. Hence, by changing the oxygen level for the same stagnation temperature, different freestream densities can be measured (compare Fig. 8). This opens a two-dimensional test area for the plasma and the collision frequency: the collision frequency (10) is dominated by the overall number density of particles, which correlates with the freestream density and the plasma frequency (9) follows the electron production and thus ionization and temperature. Besides that, the 21 vol% runs (air) resemble the conditions from [3] to have a reference. The covered parameter ranges besides freestream density and stagnation temperature are given in Table 2.

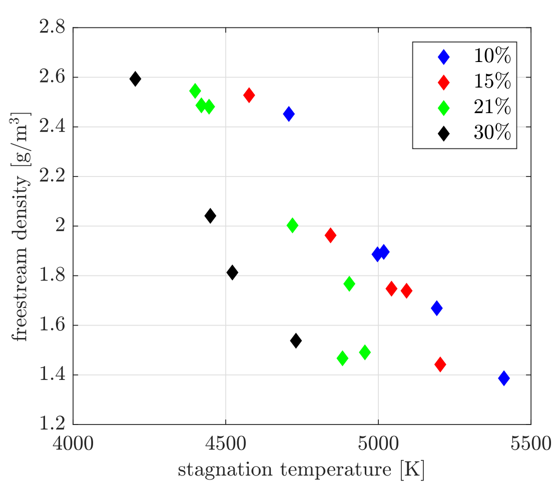

Fig. 8. The established test conditions.

Table 2
The covered range of freestream conditions.

Parameter	Range
h	$6.2\,\mathrm{MJ\,kg^{-1}}$ to $8.3\,\mathrm{MJ\,kg^{-1}}$
T_0	4204 K to 5411 K
p_∞	2.4 Pa to 3.2 Pa
ρ_∞	$1.4\,\mathrm{g\,m^{-3}}$ to $2.6\,\mathrm{g\,m^{-3}}$
T_∞	423 K to 668 K
u_∞	$3437\,\mathrm{m\,s^{-1}}$ to $3889\,\mathrm{m\,s^{-1}}$
Ma_∞	7.5 to 8.5

4. Aerodynamic simulation (CFD)

For the numerical simulations of the flow-field—comprising species concentrations and the temperatures necessitated by the electromagnetic simulation model—the OpenFOAM finite-volume method solver “hy2foam” [30] of the simulation framework “hyStrath” [38] was used.

The simulation domain comprises the nozzle supply chamber, the de Laval nozzle, and the test-section of the shock tunnel as well as the spherical model geometry on the shock tunnel centerline. A numerical axisymmetric grid of 170×10^3 prismatic computational cells, as shown in Fig. 9, was generated. Both, the tunnel wall and the sphere wall are modeled as isothermal at the ambient temperature of the laboratory of 293.5 K. At the inlet, the total pressure, temperature and species concentrations derived from the experimental conditions are prescribed. They are calculated by a thermal equilibrium code [39] from the fill conditions of the shock tunnel as well as the measured shock velocity and pressure in the nozzle supply chamber. The velocities at the inlet as well as the velocities, pressure, and temperature at the outlet of the domain are modeled as a zero-gradient boundary conditions.

To define the initial conditions, the simulation domain is split into two domains—upstream and downstream of the diaphragm. Upstream of the diaphragm, the flow-field is initialized with the measured and calculated conditions in the nozzle supply chamber. Downstream of the diaphragm, a gas mixture of 79 vol% nitrogen and 21 vol% oxygen was applied at 293.5 K and 2 Pa. The flow velocity in both domains is initialized to zero.

The spatial discretization was chosen to be second order accurate, whereas an implicit, first-order accurate, bounded Euler scheme was used for the temporal discretization.

Example flowfield contours of the stagnation region are given in Fig. 10. They show the strong electron concentration near the stagnation point and its gradual decay downstream. High temperatures and densities and hence also large numbers of collisions appear directly behind the shock but also apart from the stagnation region. This causes smaller plasma-collision frequency ratios making the permittivity and reflectivity in this area highly variable.

4.1. Grid convergence study

To verify that our computational grid is sufficiently fine to resolve the relevant features, a grid refinement study was conducted. For this purpose, a re-fined CFD grid was created, where every single computational cell was subdivided into four cells corresponding to a the grid refinement ratio of $r_{grid} = 2$. Due to the strong sensitivity of electron and plasma production with respect to temperature and thus flow enthalpy, a high enthalpy case appears best suited to study grid convergence. Hence, the results of both grids for the condition with the highest specific enthalpy among the air cases, i.e. $h = 8.14\,\mathrm{MJ\,kg^{-1}}$, are considered along the central stagnation line directly upstream of the spherical model. The peak values and the shock standoff distance d_s are compared in Fig. 11.To quantify the convergence error, Roache’s Grid Convergence Index (CGI) methodology is applied [40]. The CGI of the coarser grid among a set of two is defined as

$$CGI := \frac{F_s|\epsilon| r_{grid}^{p_{grid}}}{r_{grid}^{p_{grid}} - 1} \cdot 100\,\%, \tag{19}$$

$$\text{with} \quad \epsilon := \frac{q_{coarse} - q_{fine}}{q_{fine}}, \tag{20}$$

the default safety factor for two grids $F_s = 3$, the theoretical second order convergence of a CFD simulation, hence $p_{grid} = 2$, and q as a placeholder for the quantity under test. The results are given in Table 3. The CGI shows good convergence for the shock standoff distance and the vibrational-electronic temperature. Translational-rotational temperature, pressure and electron density are certainly not ideal but reasonable. Given large computational effort of a finer grid and the large

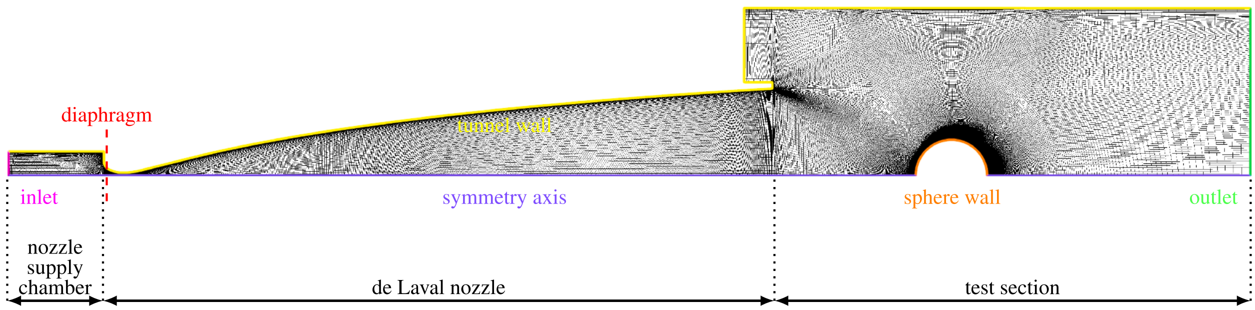

Fig. 9. Computational grid with 170×10^3 cells, the diaphragm position marks the boundary between the two different initial-conditions up- and downstream of this position to model the nozzle start-up when the diaphragm ruptures.

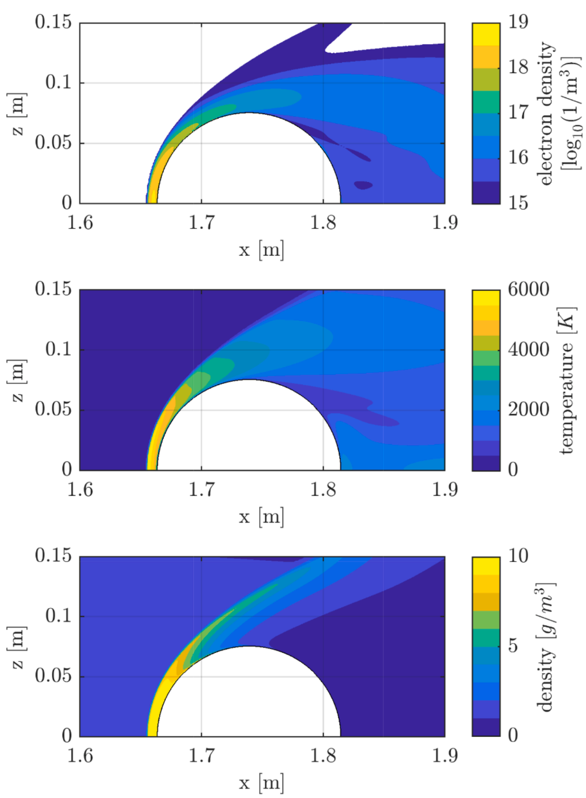

Fig. 10. Example flow field contours for a test at h =8.14 MJ kg^{-1}.

Table 3
CGI for the different peak values.

Parameter	p	T_t	T_v	$n(e^-)$	d_s
CGI [%]	23.7	11.0	4.2	54.6	4.4

number of simulations, the reasonable convergence on the coarse grid is accepted and it is used subsequently to inform the CEM simulation.

5. Electromagnetic simulation (CEM)

The plasma and collision frequencies are calculated from the CFD solution for each wind tunnel run via (8), (9) and (10). As discussed in Section 3, the Tx1 and Rx1 antennas were vertically polarized while Tx2 and Rx2 had horizontal polarization. Accordingly, two plane wave excitations were setup from the Tx1 and Tx2 directions. Receivers were placed under the angles of Rx1 and Rx2. The respective angles are given in Table 1. The computational mesh consisted of 177×10^6 block structured cells with a maximum size of 1.3 mm that resembles the one from

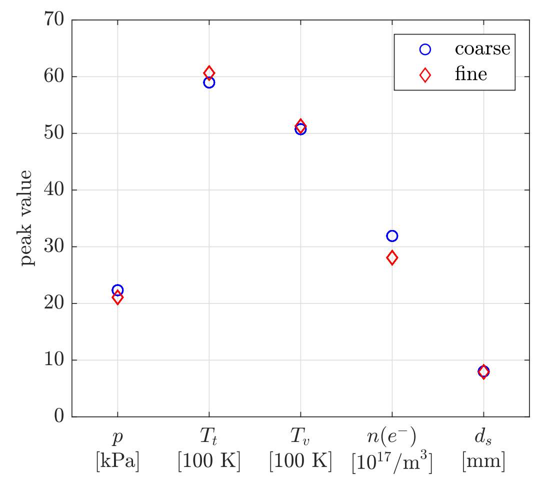

Fig. 11. CFD mesh convergence.

Table 4
Grid parameters for the CEM convergence study.

Grids	No. of cells	size [mm]
1	421×10^6	(0.81 ± 0.19)
2	177×10^6	(1.11 ± 0.24)
3	53×10^6	(1.62 ± 0.37)

[3]. In agreement with the transmitted bandwidth, the simulation applies a Gaussian frequency sweep excitation within the 3 GHz to 15 GHz range. From the scattered field the complex farfield RCS is calculated using a commercial Finite Difference Time Domain (FDTD) solver provided by CST Studio Suite. For documentation see [41]. Via Fourier transform, the RCS spectra are transformed into range profiles that can be compared directly with the measured profiles.

5.1. Grid convergence study

To verify the grid convergence, Roache's methodology has been adopted again. This time, however, the convergence study includes three grids (see Table 4). The CGI on the finer grid is used [40]

$$CGI := \frac{F_s|\epsilon|}{r_{grid}^{p_{grid}} - 1} \cdot 100\,\%, \tag{21}$$

with $F_s = 1.25$ as default. For the two adjacent grid combinations we get for the front reflection RCS (Fig. 12) the following error estimates

$$CGI_{12} = 0.16\,\% \quad \text{and} \quad CGI_{23} = 0.56\,\%. \tag{22}$$

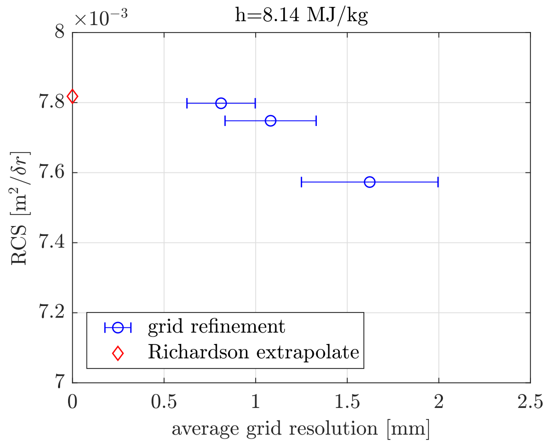

Fig. 12. CEM mesh convergence.

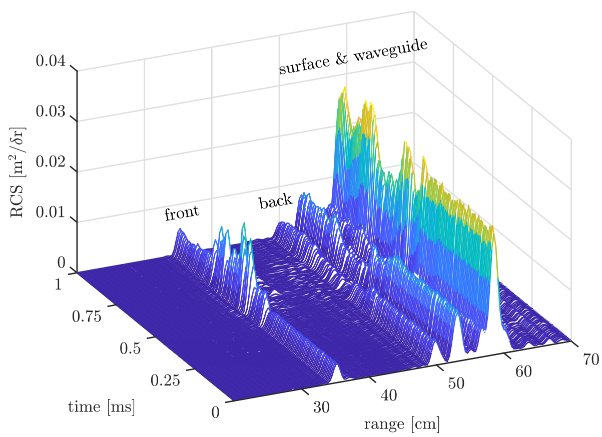

Fig. 13. A typical temporal evolution of the measured range profiles from the first test set (from [3]). The test time was between 0.6 ms and 0.7 ms.

The order of convergence was found to be $p_{grid} = 3.5$ and since

$$\frac{GCI_{23}}{r_{grid}^{p_{grid}} CGI_{12}} = 1.0032 \tag{23}$$

is close to 1, the solutions are well within the asymptotic range of convergence. Grid 2 is seen as a good compromise between computational effort and accuracy and is hence used subsequently.

6. Experimental results

As this study aims to reproduce and extend the results of the authors' prior experiments [3] with an improved setup and higher accuracy, comparability is paramount. To enable this, the procedure is again similar. Fig. 13 shows a typical sequence of radar range profiles of the hollow dielectric sphere with a first reflection at the front near 35 cm range, a reflection at the back near 50 cm and some surface wave and waveguide effects following behind. Again, to avoid any interaction between the different effects, we focus on the front reflection only—both for the simulation and the experiment.

6.1. Observations

The measured and simulated RCS of the front reflection for the two monostatic channels Tx1Rx1 and Tx2Rx2 are given in Fig. 14. First, despite an offset of approximately 0.5 dB, the measured backscatter data without flow shows good quantitative agreement with the simulations indicating a good calibration. Second, while the Tx2Rx2 channel (≈80°broadside) simulation lies within the scatter of the measurement, it makes quantitative conclusions difficult, apart from the fact that here the plasma generation has only small effect from broadside view. Third, although not very prominent, the measurement shows indications of the same order of RCS curves: 30 vol% O2 yielding the highest RCS at a given temperature, followed by 21 vol% O2, 15 vol% O2 and 10 vol% O2. Besides that, Channel Tx1Rx1 (≈30° broadside) shows a much weaker reflection than predicted. This effect has not been observed in [3] where good agreement was found although the conditions were very similar. Furthermore, the deviations seem to grow at higher temperatures and lower densities, respectively. Another feature is that during the test time for both channels no significant phase changes have been observed, i.e. mean($|RCS|$) ≈ |mean(RCS)|. This could indicate that in this case the surface is rather smooth and that only minor fluctuations and phase changes occur.

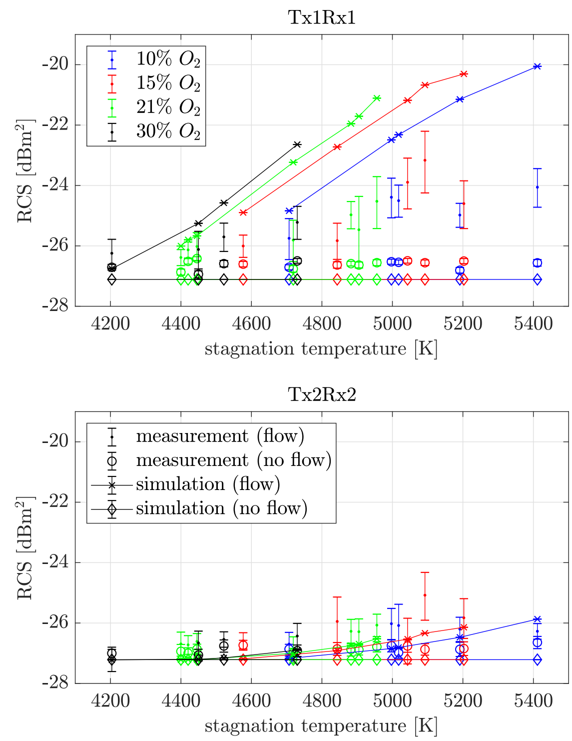

Fig. 14. The front peak RCS for the two monostatic channels Tx1Rx1 and Tx2Rx2 measured and simulated. The legend was split across both figures for better readability.

6.2. Discussion

Many cross-checks have been made to exclude systematic errors, but the deviation from the previous measurements in [3] is also visible in the raw-data. Furthermore, the measured discrepancy is far beyond the precision of the radar measurement as seen from the no flow variance in Fig. 14 and hence remains significant. The unpredicted oscillation at higher stagnation temperatures falls together with the enthalpy limit of the facility and are possibly caused by it. However, the average qualitative agreement—especially in the prediction of the onset temperature—indicates that the Drude model appears to be a good choice and that only its parameters need to be tuned.

At least for air as test gas, i.e. 21 vol%, the major differences between the prior measurements and the current ones are that the sphere was now placed a few centimeters farther away from the antenna and that the sphere placement and the antenna angle measurement was carried out with much higher precision than before. Originally, it has been especially difficult to suspend the stagnation-point into the axis of the nozzle. If the sphere had been suspended too high, it would have had a

Table 5
Potential sources of error.

Source	Eq.	Origin	Validation reference	Error estimate
$n(e^-)$	(9)	CFD	correlation with measured RAM-C II data in [3]	$\leq \pm 3\,\mathrm{dB\,m^{-3}}$ [3]
$n(s)$	(10)	CFD	assuming similar performance as for electrons	$\leq \pm 3\,\mathrm{dB\,m^{-3}}$
$\bar{v}_e$	(11)	$\bar{v}_e \approx \sqrt{\frac{8k_BT_e}{\pi m_e}}$, $T_e \approx T_{tr}$ or T_{ve} (local temperature) , CFD	CFD of a high enthalpy facility experiments [45]	$< +7.5\,\mathrm{dB\,m\,s^{-1}}$ [45]
$\pi\bar{\Omega}_{ei}^{(1,1)}$	(12) (13) (14)	[35,36]	good results for viscosity and diffusion in high temperature aerothermodynamics, however some discrepancy between different models	$\approx \pm 3\,\mathrm{dB\,m^2}$ (Fig. 15)

more central position in the antenna beam and thus also an increased RCS. This would also explain the increased no flow RCS that has actually been observed in [3]. It is hence possible, that the measured RCS in [3] was indeed overestimated. Another source of error in [3] was that the antenna angle was not measured precisely. Back then, it was estimated with 45° which in the light of the new precision measurements of the antenna also appears to be overestimated.

Besides this, surface catalycity could be another explanation for the observations as with PTFE (polytetrafluoroethene, teflon) and PA different materials have been used. It is known that the high temperatures in the stagnation point in the range of a few 1000 K can certainly erode surfaces and introduce new chemistry that is not respected here. In [7] it has been shown experimentally that material erosion can significantly affect the radar RCS. However, the erosion or ablation is a consequence of heat conduction, which takes time and shock-tunnel tests last only for a few milliseconds. Typically these time scales are too short to cause significant ablation, although tests with gallium [42] have shown that it can occur for specific materials—also in STB. For PTFE and PA no significant melting has been observed. Only small portions of surface particles left from the manufacturing process could have been eroded and evaporated. It is currently unclear whether this has a significant effect. A dedicated analysis is required, which, however, is beyond the scope of this work. But there is some evidence, that the specular front reflection in the front is not affected much by ablation [7]. This would be different if the ablation products originate from the flow generation process in the tunnel and were part of the freestream flow like remnants of the plastic diaphragm in front of the nozzle. For heat measurements such impurities have already been observed, although only in larger facilities [43]. Without further studies, this source cannot be excluded and suggests cleaner environments like ballistic ranges for testing. High speed spectrometer measurements as reported in [44] could also provide some further insights on this issue in the future.

Another factor of uncertainty is the assumption of a quasi-neutral fluid due to ambipolar diffusion, meaning locally equal numbers of electrons and NO+ ions. In low-density atmosphere, however, electrons are able to diffuse through the shock, while ions cannot as shown in [45] for freestream densities 10 to 20 times lower than in the present study. This could smoothen the otherwise sharper edge of the electron density profile and thereby reduce reflectivity. Also, the increasing deviations between the CFD-CEM model and the experimental results for the highest enthalpies and lowest densities, respectively, could be due to the ambipolar diffusion assumption getting increasingly corrupted at lower densities. Omitting the ambipolar diffusion assumption of the current simulations could hence also be insightful to better understand microwave scatter at aerodynamic plasma interfaces.

6.3. Model assessment

Now, with clear evidence that the measured discrepancy in channel Tx1Rx1 is real and assuming that ablation is insignificant, it would mean, that either the current CFD-CEM model does not produce as accurate predictions as assumed or the applied Drude model has some deficiencies. To assess this issue, the central parameters of the dispersion relation (8) are considered: the electron density $n(e^-)$, the species number density $n(s)$, the average thermal electron temperature $\bar{v}_e$ and the collsion cross-sections $\bar{\Omega}_{ei}^{(1,1)}$. For a better overview they are summarized in Table 5 and discussed below.

The electron density and thus the plasma frequency is a direct output of the CFD simulation. Discrepancies of up to $\pm 3\,\mathrm{dB\,m^{-3}}$ have been observed for the RAM C-II test case [3] and it could certainly explain part of the observed RCS increase.

If assuming similar absolute error for the number densities of the other species, their relative error would be less than for the electrons because of the higher abundance in low ionized plasmas encountered at moderate hypersonic Mach numbers below 20, hence being also $\leq \pm 3\,\mathrm{dB\,m^{-3}}$.

The average thermal electron velocity is a function of the electron temperature. It was assumed to be in equilibrium with the local average translational temperature. Though T_{ve} is probably the more correct choice, T_{tr} is in the region of interest - behind the shock - in fact very similar to T_{ve} as shown in Fig. 11. Moreover, T_{ve} was used in the previous study and is therefore used also in the following. Section 6.4 will further elucidate on the marginal effects this choice has on the overall simulated reflectivity. However, in other high enthalpy facilities partially large differences between the electron temperature and the average translational temperature have been reported [45]. Although this facility does not reach extreme enthalpies, the high temperatures in the reservoir in front of the nozzle and the following strong expansion through the nozzle could prevent the electrons from equilibrating before reaching the test volume and causing higher electron temperatures in the freestream flow. For an arc-heated wind tunnel excesses up to a factor of 30 times the ambient value have been reported [45]. This could lead to higher collision frequencies, although for the STB less deviations are expected. It would hence result in an approximate underestimation of T_e by $< +7\,\mathrm{dB\,m^{-3}}$. A progressing equilibration behind the shock could also explain the smaller differences between measurement and simulation for the broadside channel (Tx2Rx2).

Finally, the collision cross-sections also exhibit some uncertainty. Fig. 15 compares the collision frequency distribution for the $h = 8.14\,\mathrm{MJ\,kg^{-1}}$ air case from Gupta [35] with the Bottin model [36]. The Bottin model predicts clearly higher collision frequencies than the Gupta model. Under some conditions, the discrepancy exceeds even a factor of 2 and also indicates a larger collision frequency in the stagnation region. Since there is no preference except that the Bottin model is more recent, the error is estimated as $\approx \pm 3\,\mathrm{dB\,m^2}$. All error estimates are listed in Table 5.

Since the variety of possible test cases is practically infinite, general error estimates are difficult and are feasible only for distinct cases. However, this attempt tries to give an idea where the current models need improvement. To further investigate the origin of the measured

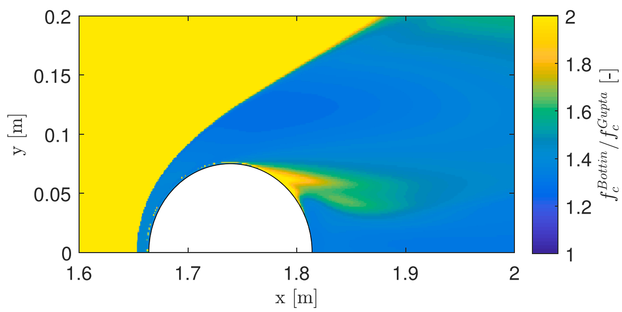

Fig. 15. The ratio of the collision frequencies for the evaluated $h = 8.14\,\mathrm{MJ\,kg^{-1}}$ case resulting from Gupta [35] and Bottin [36], respectively.

differences, a sensitivity study has been conducted. A description follows below.

6.4. Sensitivity study

Although principally every incorporated model qualifies itself as error source, the good general performance of CFD and CEM simulations indicates that the collision frequency model, the chemistry model and the aspect angle are likely ones. In order to test this hypothesis a numerical sensitivity study has been conducted that involves both the aspect angle, the collision frequency and the plasma frequency. As test case the $h = 8.14\,\mathrm{MJ\,kg^{-1}}$ case for air was chosen and allows a direct comparison with the prior data. The collision frequency distribution derived from CFD was multiplied by a factor of 0.3, 3 and 10 while the angle was varied around the aspect angle of Tx1Rx1 ($\approx 33°$). The plasma frequency was modified by a factor of 0.8, 0.6 and 0.3, corresponding to a modification of the electron density by a factor of 0.64, 0.36 and 0.09. Furthermore, the influence of using the vibrational-electronic temperature T_{ve} instead of the translational-rotational velocity T_{tr} (the current approximation) for the definition of the electron velocity v_e was tested. Also, with Bottin [36] an alternative model for collision cross-sections was considered. The results are shown in Fig. 16 and are discussed below.

First, the simulations show that the RCS decays with increasing aspect angle. This trend is found for all collision frequency factors and is also supported by the current measurement (PA-flow). A simple explanation for this dependency is that the electron density decays from the stagnation-point along the surface towards the wake flow area. By changing the aspect angle the specular reflection point is successively shifted from the nose to broadside. With it, the electron density decreases and reduces the plasma dispersion and hence the deviation from the no plasma case. Besides that, for the $1 \cdot f_c$ case the agreement of the new and the old simulation shows the consistency and repeatability of the approach.

The collection of old and new measurements does not follow this trend as already discussed above. And, given the rather poor accuracy in angle and amplitude of the 2021 measurements [3], it must be rather considered as an outlier. The higher accuracy and larger variety of cases in the present measurement induces a much higher confidence here.

The simulated angular variation around 33° also shows that the angular uncertainty is by far not large enough to explain the large observed differences in RCS at 33°.

The simulations also indicate that a collision frequency that were a factor between 5 and 7 larger would explain the measured discrepancy. An observation that is supported by the potential underestimation of the electron temperature reported in [45] and the uncertainty about the collision cross-sections comparing between the available correlations from Gupta [35] and Bottin [36] as shown in Fig. 15.

To test this assumption, the collision cross-section models and dummyTXdummy– the electron temperature approximations have been varied (cf. Fig 16). The observed effects are not large enough to explain the measured difference in RCS. This gives rise to another question, namely whether the collsion frequency in the Drude model is an angular frequency in rad or a rate in Hz. A change from a rate to angular frequency would introduce a factor of 2π which falls into the range between 5 and 7. However, the derivation as given in [34] indicates that it is rather a rate and only a classical approximation. It appears hence helpful to study more rigorous treatments. Among others, in his review article from 1977 [46], Papadopoulos mentions effectively higher collision frequencies in the context of anomalous plasma resistivity. This prediction matches the present observations and could be a possible explanation for the measured deviations. Due to its complexity, however, further investigations appear to be beyond the scope of the current work and must thus be left for future work.

Another explanation of the large deviation are deficiencies in the calculation of the electron number density. One third of the original elec-

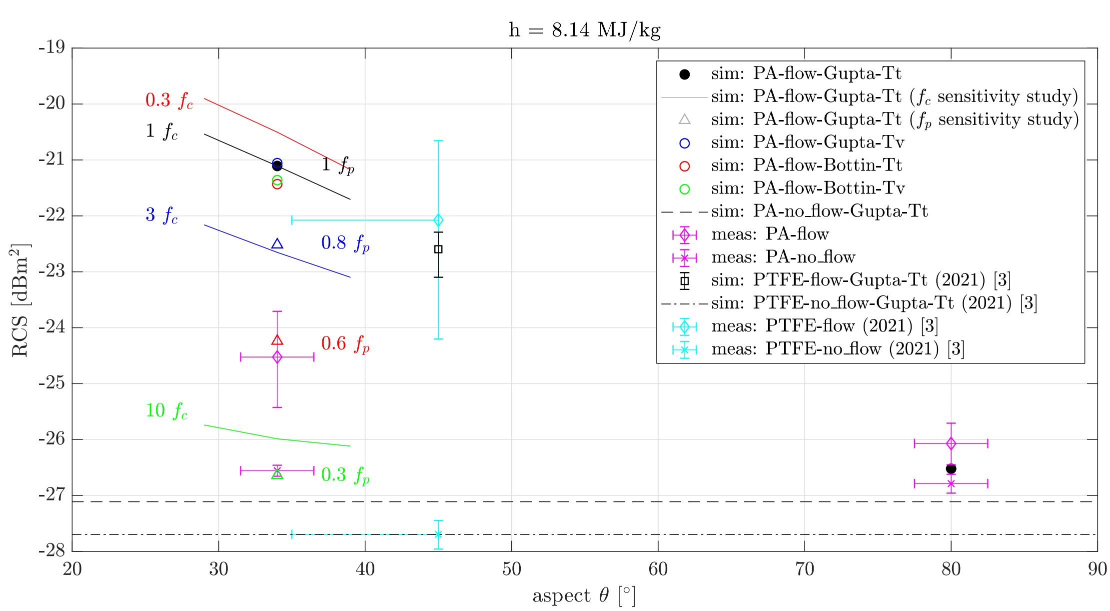

Fig. 16. A sensitivity study of the radar backscatter with respect to changes in the collision frequency. The nomenclature of the simulations: (material)-(flow/no flow)-(collision cross-section model)-(electron temperature approximation). The gray color in the legend acts as a placeholder.

tron density would produce values close to the measured RCS. Similar uncertainties have been found for the comparison of RAM C-II simulations [3].

6.5. Effects on the RCS

As shown, there are partly considerable uncertainties in the modeling parameters plasma and collision frequency (Table 5) and these affect the RCS directly as shown in Figs. 14 and 16 with a maximum difference of $\approx 3\,\mathrm{dB}$ in the considered case. While a 5 to 7 times higher collision frequency could explain the measured discrepancy (Fig. 16), the application of alternative models to derive the collision frequency did not have the desired effect. And, it is by no means clear that only the prediction of the collision frequency needs improvement. A modification of the electron density down to $36\,\%$ yields the same result and a radar measurement can only measure the effect of the local permittivity, which always incorporates both the plasma and collision frequency. To effectively separate both contributions and validate the given models, it would help to measure the electron density independently from the radar measurements. Also more rigorous treatments might help, e.g. [46].

7. Conclusion

In this study, the RCS measurements of a dielectric $15\,\mathrm{cm}$ sphere in ISL's STB shock-tunnel from [3] have been repeated with higher accuracy and additional antennas. Like before, the measurements were accompanied by respective simulations for reference. But unlike before, the good quantitative agreement could not be confirmed. Instead, the measurements revealed significant differences from the simulations. Therefore, potential error sources were identified and assessed. In a numeric sensitivity study the influence of the angle of incidence and the collision frequency was investigated. It was found that measurement errors cannot explain the large difference, while changes to the model can. Especially, the interpretation of the collision frequency as a angular frequency instead of a rate appears promising but arbitrary. If assuming that the Drude model for plasma dispersion is applicable, this means that its constituents, i.e. the plasma and collision frequency and with it the prediction of the electron density, the species number densities, the electron temperature and the collision cross-sections exhibit some inaccuracy. In order to improve the models additional test and validation is necessary—preferably in a cleaner environment like a ballistic range as done in [7].

A promising approach is to combine radar measurements with an independent technique to measure the electron density directly to separate the different contributions effectively. Although, this has been attempted by using the different oxygen levels in the present experiment, the measured discrepancy between measurement and simulation was too large to draw reasonable conclusions. Using a different facility like a ballistic range could also be a solution. Here, the uncertainty about the electron temperature and freestream impurities would practically vanish, as the models are fired into practically clean equilibrium air. It would mitigate two major error sources and probably provide more reliable reference data. Also, a review of better dispersion models (e.g. [46]) could help to solve the ambiguity about the definition of the collision frequency and yield further improvement.

Declaration of generative AI and AI-assisted technologies in the writing process

During the preparation of this work the authors used FhGenie in order to improve the language in parts of the work. After using this service, the authors reviewed and edited the content as needed and take full responsibility for the content of the publication.

CRediT authorship contribution statement

René Petervari: Writing – review & editing, Writing – original draft, Visualization, Validation, Resources, Project administration, Methodology, Investigation, Formal analysis, Data curation, Conceptualization; **Stephan Weidner:** Writing – review & editing, Writing – original draft, Visualization, Investigation; **Konstantinos Psarras:** Investigation; **Flavien Denis:** Writing – review & editing; **Peter Knott:** Writing – review & editing.

Data availability

Data will be made available on request.

Declaration of competing interest

The authors declare that they have no known competing financial interests or personal relationships that could have appeared to influence the work reported in this paper.

Acknowledgements

The authors like to thank ISL's shock-tunnel laboratory team for the conduction of the experiments and the colleagues Sebastian Karl, Volker Hannemann and Tobias Ecker (German Aerospace Center, DLR) for their support in the interpretation of the results and Salomon Arend (TNO) for his literature recommendations on anomalous plasma resistivity.

References

[1] M. Gunar, R. Mennella, Signature studies for a re-entry system (1965).

[2] E.D. Gillman, J.E. Foster, I.M. Blankson, Review of Leading Approaches for Mitigating Hypersonic Vehicle Communications Blackout and a Method of Ceramic Particulate Injection Via Cathode Spot Arcs for Blackout Mitigation, Technical Report, 2010.

[3] R. Petervari, S. Weidner, A. Nekris, S. Brüggenwirth, P. Knott, The measurement of Radar-Plasma-signatures in a hypersonic shock tunnel: simulation and experiment, IEEE Trans. Aerosp. Electron. Syst. (2023) 8581–8597.

[4] S. Esposito, A. Scarabosio, G. Vecchi, D. D'Ambrosio, Non-equilibrium plasma distribution in the wake of a slender blunted-nose cone in hypersonic flight and its effect on the Radar cross section, Aerosp. Sci. Technol. (2024) 109699.

[5] T. Lin, L. Sproul, D. Hall, J. Sontowski, Reentry plasma effects on electromagnetic wave propagation, in: 26th Plasmadynamics and Lasers Conference, 1995, p. 1942.

[6] D. Mather, J. Pasqual, J. Sillence, P. Lewis, Radio frequency (RF) blackout during hypersonic reentry, in: AIAA/CIRA 13th International Space Planes and Hypersonics Systems and Technologies Conference, 2005, p. 3443.

[7] K. Psarras, R. Petervari, F. Denis, T. Ecker, F. Kessel, P. Knott, Measuring the Influence of Ablation on Hypersonic Plasma Trails in ISL'S Hyperballistic Tunnel by Means of Radar: Simulation and Experiment, in: 59th 3AF International Conference on Applied Aerodynamics, 24th-26th March 2025, Strasbourg, France, 2025.

[8] H. Sun, J. Wang, Y. Han, Z. Cui, P. Sun, X. Shi, W. Zhao, Backward scattering characteristics of a reentry vehicle enveloped by a hypersonic flow field, Int. J. Antennas Propag. 2018 (2018) 5478580.

[9] Y. Takahashi, Propagation path of radio waves in nonequilibrium reentry plasma around a nanosatellite with an inflatable aeroshell, IEEE Trans. Aerosp. Electron. Syst. 58 (5) (2022) 4070–4082. https://doi.org/10.1109/TAES.2022.3158625

[10] J. Hao, J. Wang, C. Lee, Numerical study of hypersonic flows over reentry configurations with different chemical nonequilibrium models, Acta Astronaut. 126 (2016) 1–10.

[11] Q. Niu, Z. Yuan, S. Dong, H. Tan, Assessment of nonequilibrium air-chemistry models on species formation in hypersonic shock layer, Int. J. Heat Mass Transf. 127 (2018) 703–716.

[12] G.V. Candler, Rate effects in hypersonic flows, Annu. Rev. Fluid Mech. 51 (2019) 379–402.

[13] P. Sawicki, R.S. Chaudhry, I.D. Boyd, Influence of chemical kinetics models on plasma generation in hypersonic flight, AIAA J. 60 (1) (2022) 31–40.

[14] W. Zhang, Z. Zhang, X. Wang, T. Su, A review of the mathematical modeling of equilibrium and nonequilibrium hypersonic flows, Adv. Aerodyn. 4 (1) (2022) 38.

[15] H.-C. Deng, X. Wei, H.-C. Yin, EM scattering analysis of complex target coated with plasma by conformal SO-FDTD method, in: 2013 IEEE International Conference on Green Computing and Communications and IEEE Internet of Things and IEEE Cyber, Physical and Social Computing, IEEE, 2013, pp. 1538–1541.

[16] C. Shao, L. Nie, W. Chen, Analysis of electromagnetic scattering characteristics for a HTV-2 type flight vehicle ablation flows, in: AIP Conference Proceedings, 1628, American Institute of Physics, 2014, pp. 1277–1283.

[17] J.-W. Qian, H.-L. Zhang, M.-Y. Xia, Modelling of electromagnetic scattering by a hypersonic cone-like body in near space, Int. J. Antennas Propag. 2017 (1) (2017) 3049532.

[18] A. Scarabosio, J.L.A. Quijano, J. Tobon, M. Righero, G. Giordanengo, D. D'Ambrosio, L. Walpot, G. Vecchi, Radiation and scattering of EM waves in large plasmas around objects in hypersonic flight, IEEE Trans. Antennas Propag. 70 (6) (2022) 4738–4751.

[19] P.S. Lykoudis, A review of hypersonic wake studies (RM-4493-ARPA), Technical Report, The RAND Corporation, Santa Monica, CA, USA, 1965.

[20] G. Pippert, On the structure of wake turbulence deduced from field Radar measurements, in: Conference on Physics of Entry into Planetary Atmospheres, 1963, p. 446.

[21] H.M. Musal, R.I. Primich, W.E. Blore, Millimeter Radar instrumentation for studying plasma effects associated with hypersonic flight Technical Report No. TR64-02J, GM Defense Research Laboratories, Santa Barbara, CA, 1964.

[22] D.W. Boyer, S.N. Andre, Theoretical and Experimental Studies of Microwave Interaction Effects in a Hypersonic Air Plasma., Technical Report, Cornell Aeronautical Lab., Inc., Buffalo, NY, 1972.

[23] R. Petervari, A. Nekris, T. Bieker, Numerical Analysis of Radar-Plasma-Signatures of aSphere in a Mach 10 Hypersonic Wind Tunnel Flow, in: 2021 18th European Radar Conference (EuRAD), 2022.

[24] D.G. Fletcher, Fundamentals of Hypersonic Flow-Aerothermodynamics, Technical Report RTO-EN-AVT-116, 2005.

[25] J.D. Anderson Jr., Hypersonic and High-Temperature Gas Dynamics, AIAA, 2019. 3rd edition.

[26] C. Park, Review of chemical-kinetic problems of future NASA missions. I-Earth entries, J. Thermophys. Heat Transfer 7 (3) (1993) 385–398.

[27] R.C. Millikan, D.R. White, Systematics of vibrational relaxation, J. Chem. Phys. (12) (1963) 3209–3213.

[28] J. Appleton, K. Bray, The conservation equations for a nonequilibrium plasma, J. Fluid Mech. 20 (4) (1964) 659–674.

[29] S. Weidner, Y. Hoarau, J.-D. Parisse, F. Leopold, Assessment of numerical simulation tools for hypersonic non-equilibrium flow-fields, in: 57th 3AF International Conference on Applied Aerodynamics, 3AF, Bordeaux, France, 2023. AERO2023-26.

[30] V. Casseau, R.C. Palharini, T.J. Scanlon, R.E. Brown, A two-temperature open-source CFD model for hypersonic reacting flows, part one: zero-dimensional analysis, Aerospace 3 (4) (2016) 34.

[31] R.N. Gupta, J.M. Yos, R.A. Thompson, A Review of Reaction Rates and Thermodynamic and Transport Properties for the 11-Species Air Model for Chemical and Thermal Nonequilibrium Calculations to 30000 K, Technical Memorandum 101528, Hampton, VA, 1989.

[32] F.G. Blottner, M. Johnson, M. Ellis, Chemically Reacting Viscous Flow Program for Multi-Component Gas Mixtures, Technical Report SC-RR-70-754, Albuquerque, NM, USA, 1971.

[33] B.F. Armaly, K. Sutton, Viscosity of multicomponent partially ionized gas mixtures, in: 15th Thermophysics Conference, Snowmass, CO, July 14–16, 1980.

[34] A. Piel, Plasma Physics: an Introduction to Laboratory, Space, and Fusion Plasmas, Springer, 2017.

[35] R.N. Gupta, J.M. Yos, R.A. Thompson, K.P. Lee, A review of reaction rates and thermodynamic and transport properties for an 11-species air model for chemical and thermal nonequilibrium calculations to 30000 K, NASA1232, 1990.

[36] B. Bottin, Aerothermodynamic model of an inductively-coupled plasma wind tunnel, Ph.D. thesis, Von Karman Inst. Fluid Dynam., 1999.

[37] O. Igra, F. Seiler (Eds.), Experimental Methods of Shock Wave Research, 478, Springer, 2016.

[38] V. Casseau, An open-source CFD solver for planetary entry, Ph.D. thesis, University of Strathclyde, 2017.

[39] M.K. McIntosh, Computer Program for the Numerical Calculation of Frozen and Equilibrium Conditions in Shock Tunnels, Technical Note CPD, 1968.

[40] P.J. Roache, Verification and Validation in Computational Science and Engineering, 895, Hermosa Albuquerque, NM, 1998.

[41] D. Systèmes, CST Microwave Studio, CST Studio Suite Documentation, 2023.

[42] F. Denis, Study of the Ablation by Melting in Hypersonic Flow, Ph.D. thesis, Université de Strasbourg, 2022.

[43] B.A. Cruden, C.Y. Tang, J. Olejniczak, A.J. Amar, H. Tanno, Characterization of radiative heating anomaly in high enthalpy shock tunnels, Exp. Fluids 62 (7) (2021) 142.

[44] D. Ramjaun, M. Dumitrescu, R. Brun, Kinetics of free radicals behind strong shock waves, J. Thermophys. Heat Transfer 13 (2) (1999) 219–225.

[45] M. Kim, A. Gülhan, I.D. Boyd, Modeling of electron energy phenomena in hypersonic flows, J. Thermophys. Heat Transfer 26 (2) (2012) 244–257.

[46] K. Papadopoulos, A review of anomalous resistivity for the ionosphere, Rev. Geophys. 15 (1) (1977) 113–127.